Journal of Physics: Conference Series

PAPER • **OPEN ACCESS**

Riga Group's recent results on laser applications for skin diagnostics

To cite this article: J Spigulis *et al* 2021 *J. Phys.: Conf. Ser.* **1859** 012033

View the article online for updates and enhancements.

This content was downloaded from IP address 5.179.12.136 on 12/04/2021 at 10:28

Riga Group's recent results on laser applications for skin diagnostics

J Spigulis*, V Lukinsone, I Oshina, E Kviesis-Kipge, M Tamosiunas and A Lihachev

Biophotonics Laboratory, Institute of Atomic Physics and Spectroscopy, University of Latvia, Jelgavas 3, Riga, LV-1004, Latvia

*E-mail: janis.spigulis@lu.lv

Abstract. The laser-related activities are reviewed of the Biophotonics Laboratory at UL Institute of Atomic Physics and Spectroscopy following the previous ICSQE-2018 conference. Four recent research projects are considered, including one EC Horizon-2020 project, two European Regional Development Fund (ERDF) projects and one project funded by the Latvian Council of Science (LCS). The projects are generally aimed at developing new optical methods and technologies for non-invasive *in-vivo* skin assessment to facilitate the early diagnostics of skin malformations (including cancers). Most of the projects explore novel approaches of camera-based biomedical imaging to the clinical diagnostics and recovery monitoring.

1. Introduction

A brief review will be presented of the Biophotonics Laboratory activities on lasers for skin assessment following the previous ICSQE-2018 conference. The main ongoing projects are:

1) *Multimodal imaging technology for in-vivo diagnostics of skin malformations*, ERDF #1.1.1.1/18/A/132;
2) *Development of prototype devices for non-invasive assessment of skin condition*, ERDF #1.1.1.2/VIAA/1/16/070;
3) *Time-resolved autofluorescence methodology for non-invasive diagnostics of skin cancer*, ERDF #1.1.1.2/VIAA/1/16/014;
4) *Advanced spectral imaging technology for skin diagnostics*, LCS # lzp-2018/2-0006.

The first project aims at developing a combined method for skin diagnostics involving picosecond laser applications for time-dependent optical characterization of skin (autofluorescence lifetimes, fluorescence lifetime imaging, time-of-flight spectroscopy, skin-remitted photon path lengths). Values of the remitted photon path lengths at particular wavelengths and input-output distances are important for several clinical applications, including reflection pulse oximetry and skin chromophore mapping. They can be estimated by modelling; however, there are very few experimental data available to validate the simulations. Models mostly consider distribution of path lengths for all photons independently of their travel directions and interactions within the tissue. One can expect that the total path length of the survived skin-remitted photons should be longer than the mean path length related to all photons launched in the tissue (where a certain amount of them is absorbed). Systematic experimental studies on the spectral and spatial dependencies of the skin-remitted photons are needed to quantitatively answer this question. Our measurements were taken using specific optical fiber contact probes from *in-vivo*

Content from this work may be used under the terms of the Creative Commons Attribution 3.0 licence. Any further distribution of this work must maintain attribution to the author(s) and the title of the work, journal citation and DOI.
Published under licence by IOP Publishing Ltd

skin, both healthy and pathologic, and from agar-based skin phantoms. Besides, Raman spectra and Raman spectral band images from ex-*vivo* skin samples under 785-nm laser excitation were studied in framework of the first project.

In the second and fourth projects, different concepts of multi-spectral-line imaging are implemented in new prototype devices for skin chromophore mapping and autofluorescence imaging. One design comprises an illumination ring of laser diodes around the image capturing camera. Another one employs a silica-core side emitting fiber loop as a simultaneous four spectral line illumination source, combined with a double-camera setup or with a single VIS-NIR four-band camera. Besides, skin autofluorescence is excited by violet 405-nm laser diodes and detected in the G-band of an RGB camera. Unfortunately, the clinical validation phase of the prototypes is somewhat delayed due to restrictions related to the Covid-19 pandemic. The third project investigates origins of the photo-bleaching of laser-excited skin autofluorescence.

2. Methods and Equipment

In the first project, the measurement set-up shown in figure 1 was used. The time-correlated single photon counting method was applied for optical pulse shape measurements. A broadband picosecond laser (Whitelaser micro supercontinuum lasers, Fianium, NKT PHOTONICS, DK, 400-2000 nm, pulse full width at half maximum 6 ps, repetition rate 20 MHz) was used as an initial light source. The time resolution of the system was 9.7 ps which ensured a minimum detectable photon path length of ~2 mm. Specific narrow spectral bands were selected by couples of identical interference filters. One of them was filtering the input light while the other was placed in front of the photo-detector (photomultiplier HPM-100-07 combined with the detector controller DCC-100 and data processing card SPC-150, all Becker&Hickl GmbH, DE). The estimated the temporal resolution of the system was ~5 ps, which causes an ~1-mm error of the determined photon path lengths. The examined spectral range was 560 – 800 nm; the spectral bands were selected with a 40-nm step using 10-nm half-bandwidth interference filters (Andover Corporation, USA - part numbers 560FS10-12,5; 600FS10-12,5; 640FS10-12,5; 680FS10-12,5; 720FS10-12,5; 760FS10-12,5; 800FS10-12,5).

Stable recording of optical signals via the input and output fibers (WF-400, Light Guide Optics International, LV, silica core diameter 400 microns, length 1,05 m) was ensured by means of a custom-made fiber holding probe with inter-fiber distances 1 mm, 8 mm, 12 mm, 16 mm and 20 mm. To provide equal pressure on the skin surface in all measurements, the probe was designed as a lift where the inside sliding part with the couple of fibers lied on the skin, providing a pressure determined by its weight ~35 g/cm^2. The outside part of the probe was fixed on skin during the measurements. In order to

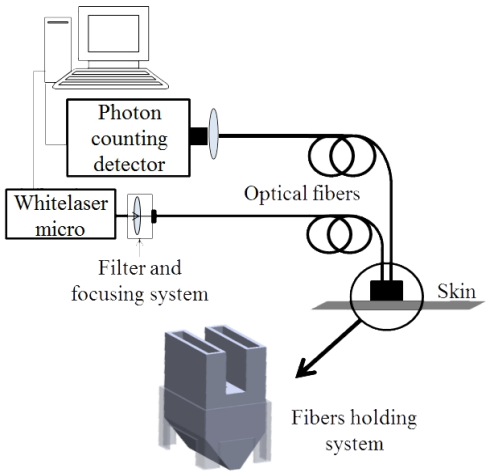

Figure 1. The picosecond pulse reflectance measurement set-up.

verify how much variation the probe pressure causes in the mean photon path lengths, additional series of measurements at two wavelengths (760 nm and 800 nm) and all five inter-fiber separations were taken applying three probe-skin pressures – 35 g/cm^2, 112 g/cm^2 and 224 g/cm^2. The variations observed did not exceed 5 %.

Ten volunteers with skin photo-type II or III (Fitzpatrick classification), aged between 25 and 68, were examined with their written consent under permission of the local Ethics Committee. The measurements were taken from healthy skin of the forearm, avoiding contact with large superficial blood vessels. The average spectral power on skin was ~10 mW/cm^2, i.e. well below the skin laser safety limit of 200 mW/cm^2 [1].

Processing of the measured data involved comparing the shapes of skin input and output pulses, *a(t)* and *b(t)*, respectively. The temporal distribution function *f(t)* of photon arrivals following an infinitely narrow δ-pulse input were found by de-convolution of the integral

$$b(t) = \int_0^t a(t-\tau) f(\tau)\, d\tau \quad (1).$$

This inverse problem was solved using a built-in deconvolution algorithm of Matlab. As the de-convolved function was more noisy than *b(t)*, original scripts were developed for data smoothing using the Log-normal function, as well as for semi-automatic calculations of the temporal distribution functions and the mean arrival times of skin-scattered photons. In particular, the output signal *b(t)* was fitted by a Log-normal distribution function using the non-linear fitting Matlab lsqcurvefit algorithm. This function was selected due to its similarity to the measured data. Next, the input pulse was shifted in time towards the output pulse until the pulses' rising fronts coincided at the 5% level. The path length of the first detected photons was obtained as: *Min path length = dtc/n* , where *dt* is the time shift towards the output pulse. Then the inverse problem (1) was solved using the built-in Matlab deconvolution algorithm deconv and *f(t)* was calculated. Finally, the mean arrival time of skin-scattered photons was calculated as the time moment when the area under curve *f(t)* equals from left and right side. After restoring *f(t)*, the corresponding distribution of back-scattered photon path lengths in skin was calculated as

$$\phi(s) = f(t) \cdot c / n \quad (2),$$

where *c* is the speed of light in vacuum and *n* is the mean refraction index of superficial skin tissues (*n* ~ 1.4 [2]). The photon mean path lengths in skin were found as the mean values of integrated path length distribution functions. The possible error due to the different slopes of the two rising fronts (after the time-shifting) did not exceed 2 mm.

Recently we proposed and tested a new multispectral imaging modality where illumination of the target (e.g. skin) is performed by multiple laser-emitted spectral lines instead of spectral bands. We demonstrated that up to three spectral line images can be extracted from a single snapshot RGB image data set under simultaneous triple-wavelength illumination [3-5]. Recently, a four spectral line imaging double-camera prototype (figure 2) was designed, assembled and tested [6]. The illumination system comprised two laser modules – an RGB module emitting ~20 mW at each of the three spectral lines (450 nm, 523 nm, 638 nm), and an NIR 850 nm/40 mW module. As a patented novelty, several semi-elliptical loops of a side-emitting optical fiber attached to the laser modules were exploited as a light source ensuring uniform multi-laser illumination of the target area via a polarizing film. Two cameras (RGB and NIR, MQ022CG-CM and MQ022RG-CM respectively, Ximea, DE) equipped with 425-nm and 800-nm long-pass filters (mod. #84-742 and #66-235, Edmund Optics, GB, respectively) and orthogonally-oriented input polarizers are capturing simultaneously images of the same skin area. Four spectral line images are subsequently extracted from the image data for further calculation of four chromophore distribution maps using the previously developed methodology [7]. Within a second, the laser modules are switched off and a skin autofluorescence (AF) image at the G-channel of the RGB camera is captured under illumination by four 405-nm, 40-mW laser diodes (DL-5146-101S, Roithner, AT), in order to discriminate skin melanoma from seborrheic keratosis [8]. The recorded images can be seen on the display (5.5-inch HDMI AMOLED, Waveshare, CN) or transmitted via SBC's *wi-fi* to the

remote computer for calculation of chromophore maps or performing other tasks. The device is fully self-sustained by using rechargeable Li-ion batteries (INR18650-25R, Samsung, KR) as the power supply.

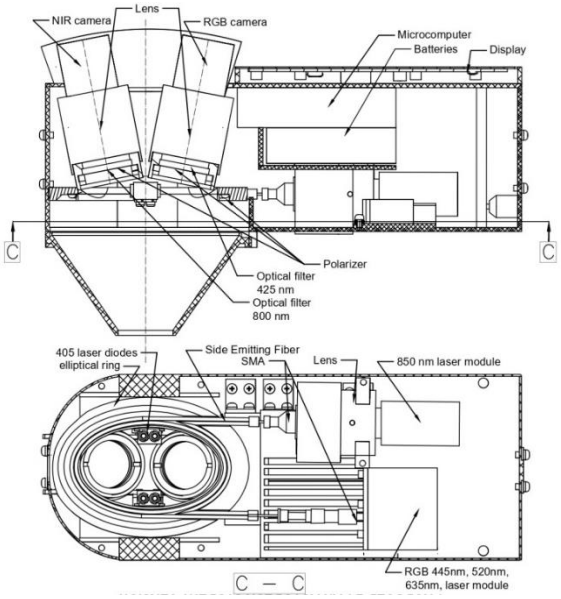

Figure 2. Design scheme of the 4+1 laser wavelengths prototype device [6].

Another recent design [9] allowed consecutive capturing of five spectral line images within four seconds using a laser diode ring illuminator (figure 3 (a)). The device functions (figure 3 (b)) based on the Windows CE 7.0 operating system; it has built-in processing software for nearly real-time calculation of skin chromophore maps. In total, 20 laser diodes emitting at five wavelengths (405 nm, 450 nm, 520 nm, 660 nm, and 850 nm) and four white LEDs for preview mode are operated. Each set of equal lasers is powered separately by a constant current laser driver. A system on chip module Nvidia Tegra 2 T20 with a 1-GHz dual core Arm Cortex-A9 processor is used as a central processing unit. A three Mpix RGB CMOS matrix serves as the image sensor connected to a central processor via a 10-bit parallel line. The image sensor has 10-bit ADC which provides1024 grades of intensities for each spectral image. A mini USB connector and a SD memory card are used for image transfer to external computer. All low level tasks are laid down to a 32-bit Arm-based Cortex®-M4 STM32L4 series microcontroller. It is programmed as an I2C interface slave device and emulates an RTC chip. Pushbutton tasks are embedded.

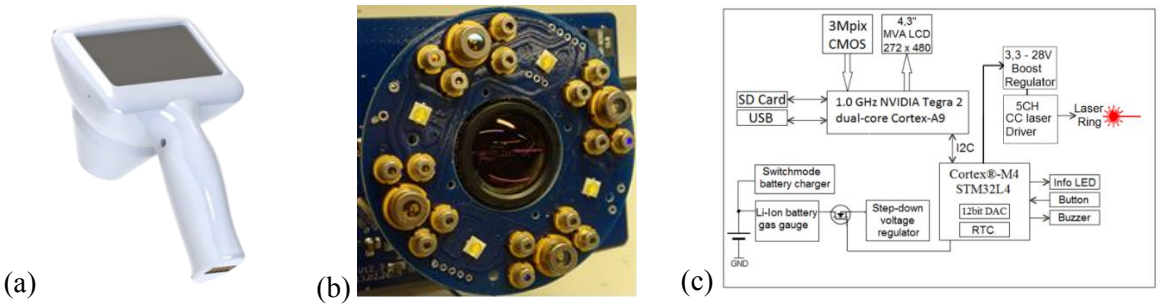

Figure 3. Outlook (a), design details (b) and functional scheme (c) of the recent five spectral line imaging prototype [9].

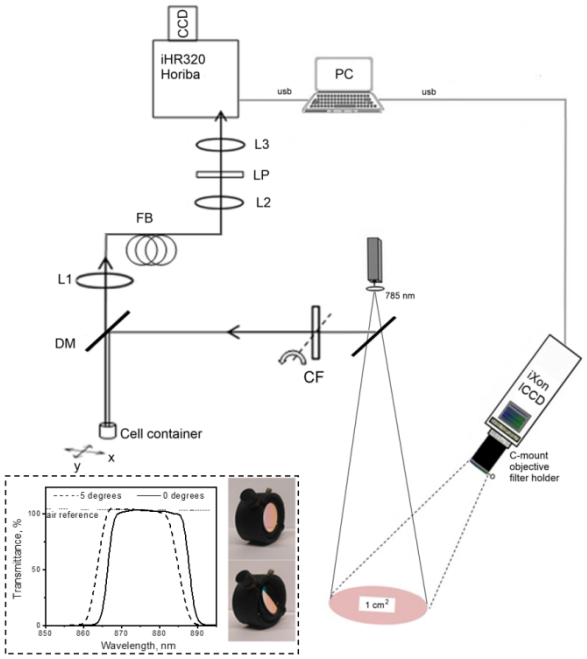

Figure 4. Combined set-up for acquisition of Raman macro-images and spectra.

An intensified CCD camera (iXon Ultra 888, Andor) records Raman images through the set of optical filters embedded into the filter holder, including a 785-nm laser rejection filter and a rotated bandpass filter positioned at 0 degrees or at 5 degrees perpendicular to the optical axis. Additional components: CF – laser clean-up filter; DM – dichroic mirror; L1 – fibre coupling lens; L2, L3 – collimating lenses; FB – fibre bundle; LP – long pass filter ($OD_{785\,nm}$>6); xy – translational stage. The transmittance spectra of the tuneable bandpass filter were measured by using DU 800 (Beckman Coulter, Brea, CA, USA) spectrophotometer software. The dimensions of the device are 121×205×101 mm^3, weight ~440 g.

A case study for non-melanoma skin cancer diagnosis was included in the Raman scattering research project. Raman spectroscopy and imaging data were obtained from human squamous cell carcinoma (SCC), basal cell carcinoma (BCC), nevus and surrounding skin samples, *ex vivo*. The Raman spectra were recorded by an iHR320 imaging spectrometer equipped with a 1200 g/mm grating and a thermoelectrically cooled Syncerity-CCD camera (Horiba, Japan). A 785-nm diode laser excitation was delivered to the sample by fibre optics used together with the filter sets to adjust the output fluence to 40 mW/cm^2 and to filter out the fiber' silica bands, including the dichroic filter serving to reflect/reject excitation light and to transmit the Raman signal (figure (4)). The imaging system comprised an iXon Ultra 888 EMCCD camera (DU-888U-CS0-#BV, Andor Technology, UK), a 785-nm excitation notch filter (NF03-785E-25, Semrock, USA) and a narrow-band optical filter (FF01-880/11-25, Semrock, USA) attached to a macro lens (35-mm focal length, f/2.8 – f/16, Edmund Optics). The angular adjustment of the narrow-band filter produced a ~3-nm anti-Stokes shift at a 90% transmittance level. The final image of the Raman scattered light was computed by subtracting two images transmitted at different peak wavenumbers, thereby removing the background autofluorescence of the sample.

The cell preparation for Raman spectroscopy and autofluorescence measurements was follows: dc-3f or b16f10 cells were cultured as a monolayer in DMEM (supplemented with 10% fetal calf serum, 1% l-glutamine, 100 µg/ml streptomycin and 100 u./ml penicillin), incubated at 37 °C with 5% CO_2 and air. Shortly before the measurements, the cells were trypsinized, re-suspended in 1x PBS, centrifuged and the pellet of approx. 6×10^6 cells was transferred into a flat-bottom cylinder container (h = 3mm, r = 2.5 mm, V = 50 µl) tightly covered inside with 24" gold foil. A fibre bundle comprising a single

excitation fibre and six collection fibres (NA = 0.22) was positioned at a 25-mm distance from the cell sample surface. To conduct the Raman spectral measurements on the dead cells, the cells were stored in PBS at 4 ºC for up to one month. To conduct autofluorescence measurements, the cells were incubated with singlet oxygen sensor green (SOSG) reagent (Promega Corp., USA) at a 5-μM final concentration and affected with light for 10 minutes at a 30-mW/cm^2 power density. The SOSG fluorescence was estimated in cell supernatant under 473-nm excitation.

3. Results

As a result of the kinetic skin remittance measurements, nearly linear dependences of the remitted photon mean path length on the inter-fibre distance were obtained for all wavelength bands, while the spectral dependences at fixed inter-fibre distances showed a more complicated nature, most probably due to absorption of the dermal haemoglobin (figure 5). More results of this study are published in [10].

Figure 6 (a) illustrates the data obtained on the photon mean path length through healthy skin and skin neoplasms. The data was calculated as the mean values from six measurements (skin and pigmented nevi of diameter 8 – 11 mm). As expected, increasing the inter-fibre distance and increasing the wavelength led to an increased photon path length. However, we did not observe essential differences in their values when healthy skin and neoplasms were compared. We noticed that the photon path length increases in body locations with more fat, which also results in an increased error in the average data for all measurements at longer wavelengths and larger distances between fibres.

Figure 6 (b) illustrates the mean photon path length dependencies in phantoms. The phantoms comprised two different concentrations of additives, the first one with 1% of intralipid concentration and the second, with 1% of intralipid and 1% of haemoglobin. The results were obtained for four wavelengths (520 nm, 560 nm, 680 nm and 760 nm) at five different distance between fibres (1 mm, 8 mm, 12 mm, 16 mm and 20 mm). Haemoglobin is the main absorber in human skin below 600 nm. As expected, in phantoms with haemoglobin the mean photon path length is shorter compared with that in phantoms without haemoglobin.

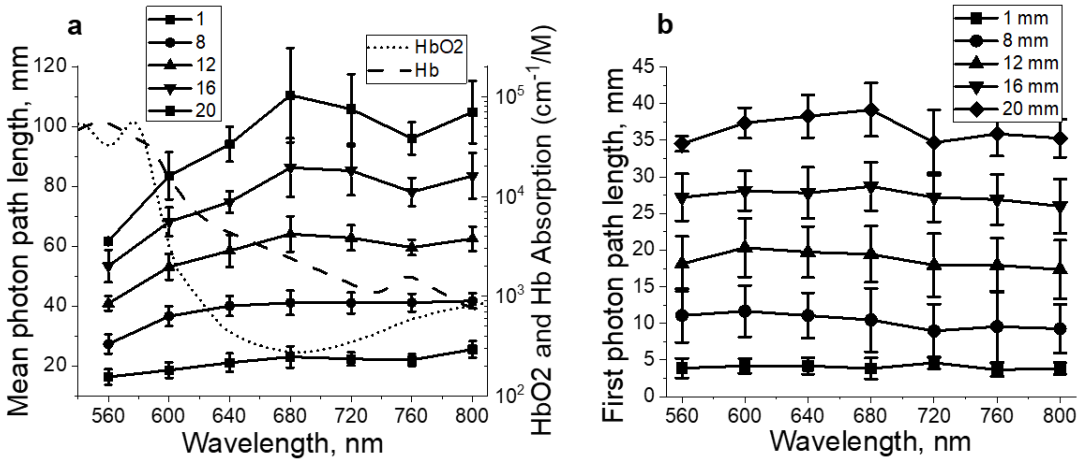

Figure 5. (a) – spectral dependencies of the mean path length of skin-remitted photons at various inter-fiber distances, (b) – spectral dependencies of the path lengths calculated for the first-arrived photons (detected at 5% level of output pulse maximum). The dotted curves in (a) represent absorption of oxy- and deoxy-haemoglobin [10].

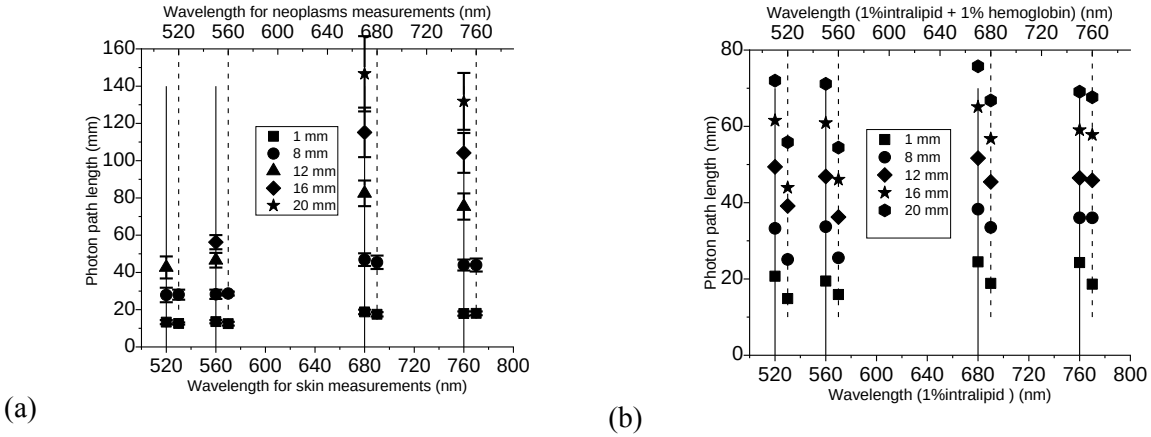

Figure 6. (a) – mean remitted photon path lengths in skin (–) and neoplasms (--); (b) – data for phantoms with 1% of intralipid concentration (–) and with 1% of intralipid and 1% of haemoglobin concentration (--) [11].

Concerning the Raman scattering results, the skin spectra obtained were composed of Raman vibrational modes of proteins, lipids, and amino acids. Skin cancer induces changes in these components, namely, reduces the Raman band intensities near 1300 cm^{-1} and 1450 cm^{-1} (figure 7). In line with the previous studies [12, 13], the Raman signal reduction in BCC and SCC skin cancer indicated lower amounts of collagen and elastin (1271 cm^{-1}, 1452 cm^{-1}), and lower contents of ceramide and triolein lipids (1301 cm^{-1}, 1440 cm^{-1}). The intensity decrease at 1450 cm^{-1} corresponds to a change in the proteins' molecular composition.

The Raman macro-imaging results confirmed the decreased Raman intensity of BCC and SCC cancer in comparison to the healthy skin (figure 8). Considering the filter transmittance at a level >90 %, the filter rotation at 0 degrees (or at 5 degrees) allows one to capture a Raman image in the 1217 – 1456 cm^{-1} (or the 1185 – 1409 cm^{-1}) wavenumber interval. Thus, the differential image extracts the Raman band intensity alterations in the 1409 – 1456 cm^{-1} wavenumber interval, particularly corresponding to the Raman band intensity decrease near 1450 cm^{-1} related to the developed skin cancer. This is explained

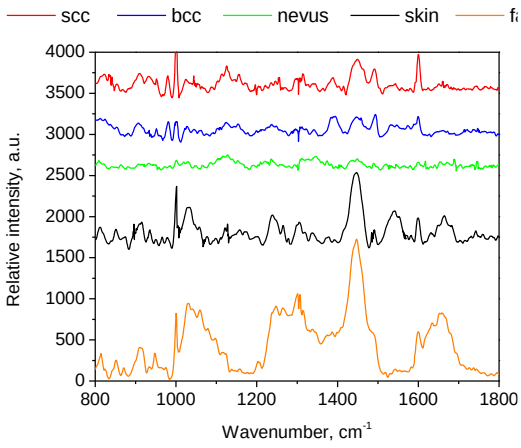

Figure 7. Measured mean Raman spectra of skin, subcutaneous fat tissue, nevus and skin cancer (SCC and BCC). The intensity axis offset is induced for clarity.

by the tumor-secreted metalloproteinases inducing a degradation of collagen and prohibiting pro-collagen biosynthesis. The smaller amount of triolein could be due to a lowering of the subcutaneous volume of fat during the lesion formation [13].

Our data also showed that the Raman spectral features of a nevus could be more likely related to BCC or SCC than to normal skin (figure 7). Thus, the imaging results are not cancer-specific, as Raman images of nevus display reduced intensity compared to the skin. However, we should emphasize that the Raman signal reduction is a temporal process, significantly affected by the occurrence of cell death. It has been shown previously that the decrease of the Raman band intensity near 1450 cm^{-1} occurs due to the cell death (necrosis) [14]. We observed that this decrease in the 1450-cm^{-1} peak intensity (dominated by proteins and lipids) is consistent with a malignant transformation, independently of the tissue type (BCC or SCC). Further results obtained *in vitro* were used to model the Raman spectral changes related to the time course of cell death. The decrease of the whole Raman spectrum intensity at 1448 cm^{-1} was observed in dead cells (figure 9). As shown in figure 9 (inset), the data points approximated by a mono-exponential decay yielded a time of nine days for the 1448-cm^{-1} band intensity to decrease to 37% of its initial value. As already described [14], the degradation of the lipid membranes occurs first, resulting in a significant decrease in the Raman intensity from lipid compounds measured in the dead cells within 24 – 72 hours. The peak residuals can be ascribed to the protein content, however, no comparison to previous work is available to relate the decrease in the Raman spectra intensity to protein and lipid structure alterations at longer times.

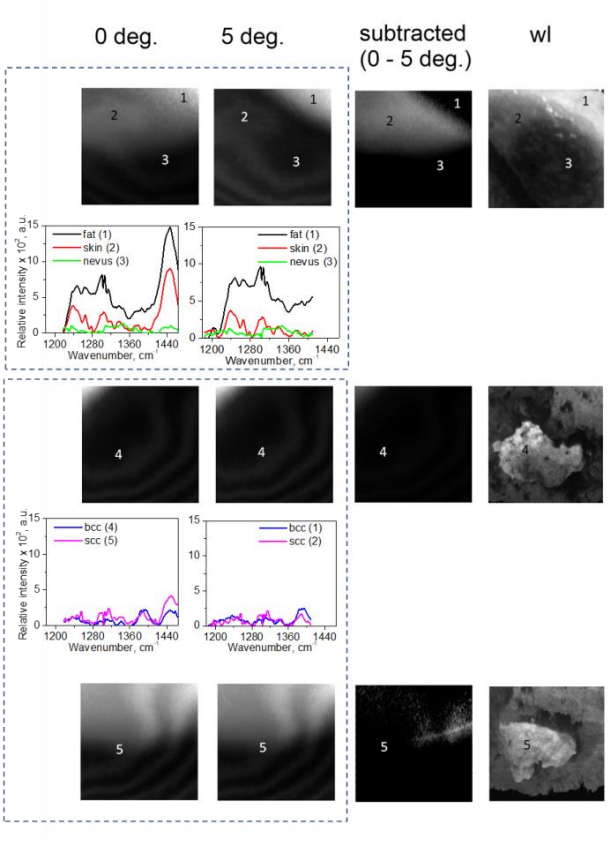

Figure 8. Top view of Raman macro-images at 0 degree and 5 degree filter rotation and white light images, *ex vivo*. The numbers on the imaging data denote morphological tissue localization: 1 – subcutaneous fat; 2 – skin; 3 – nevus; 4 – BCC; 5 – SCC. The subtracted images (5 deg. from 0 deg.). are depicted in the middle column. To interpret the relative image intensity values, the regions of interest (morphology) are co-localized with Raman spectral data.

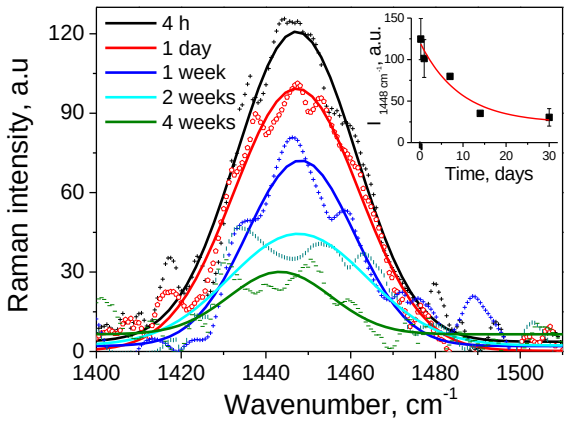

Figure 9. Differences in the Raman band intensity at 1448 cm^{-1} of live dc3-f cells and dead cells stored at 4 ºC in 1x PBS for 1 day, 1 week, 2 weeks and 4 weeks.

The literature review revealed that following laser irradiation of a biological sample, the signal-to-noise ratio of Raman spectra would increase thanks to the decreased NIR autofluorescence intensity (photo-bleaching) [15]. The mechanism of cell and tissue autofluorescence photo-bleaching is still unclear. The main hypotheses considered in the literature are: a) spontaneous fluorophore decomposition (after a number of absorption/emission cycles), b) destructive interactions with other dye-molecules and c) interaction with oxygen molecules and their derivatives. To check the hypothesis that intrinsic fluorophores in cells (NADH, flavines and lipopigments) play a role as endogenous photosensitizers with subsequent production of singlet oxygen [16], in-vitro mouse melanoma cells b16f10 with attached singlet oxygen fluorescence sensor (SOSG) were irradiated by continuous laser light (405 nm, power density of 30 mW/cm^2) for 10 minutes. The results obtained (figure 10) demonstrate opposite trends of the two fluorescence intensities over time. The decrease of the cells' autofluorescence intensity can be well described by an exponential decay with a rate constant τ_1 = 1.06 +/- 0.19 minutes, while the SOSG fluorescence intensity increase was also exponential, but slower, with a rate constant τ_2 = 2.6 +/- 1.15 minutes. One can assume that not only singlet oxygen is produced during the photo-bleaching, but also radicals, such as hydroxyl radicals, superoxide anion radicals, etc.

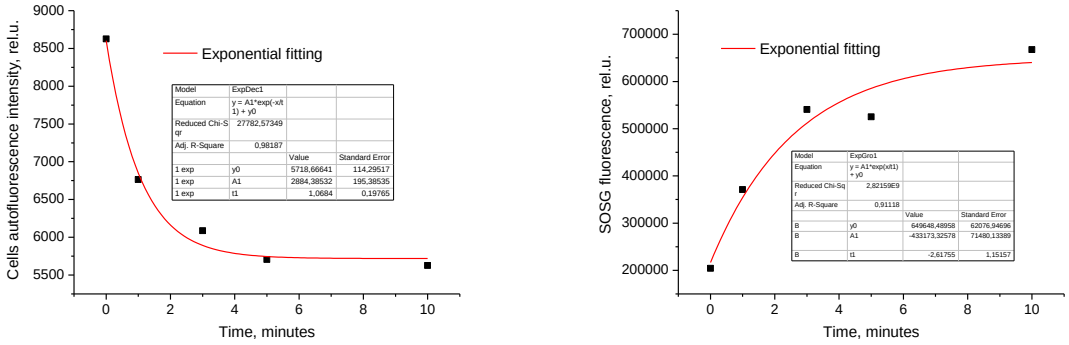

Figure 10. Left – melanoma cell autofluorescence intensity decrease during 10 minutes at 405-nm continuous excitation measured at the 480-nm band. Right – singlet oxygen fluorescence measured at the 520-nm band under 473-nm excitation in the same experiment.

4. Summary

To summarize, the recent results of our research team on laser applications for skin assessment show a promising potential of the applied biophotonic methods. Results have been reported of the first systematic experimental study to determine the spectral-spatial dependencies of skin-remitted photon path lengths by means of picosecond lasers [10]. Two design options for skin imaging with record high spectral selectivity using multi-laser illumination have been implemented in prototype devices [6,9]. A new research line – Raman skin spectroscopy and imaging – has been initiated. Raman macro-imaging can provide diagnostic criteria for the detection of skin malformations that are attributed to changes in the tissue structure and the time course of lipid or protein degradation. However, more testing is necessary to demonstrate the reliability of this method. The strength of Raman macro-imaging is the capability to provide a wide field of view (~ cm^2), fast acquisition (10 seconds/image) and safe imaging conditions (< 300 mW/cm^2 power density). This method is still too complicated and expensive for immediate clinical applications, but further research may explore ways for routine implementation in the future. Finally, the results obtained on cell fluorescence photo-bleaching (figure 10) will contribute to the better understanding of the mechanisms of skin autofluorescence photo-bleaching under laser excitation.

Acknowledgements

Authors would thank for the support provided by the European Regional Development Fund (projects No. 1.1.1.1/18/A/132, 1.1.1.2/VIAA/1/16/070 and 1.1.1.2/VIAA/1/16/014) and by the Latvian Council of Science (project No. lzp-2018/2-0006). The technical support of Dr. Ilona Kuzmina (preparation of the tissue phantoms) is highly appreciated.

References

[1] *Safety of Laser Products* 2007–Part 1: Equipment Classification and Requirements IEC 60825–1
[2] Ding H, Lu J Q, Wooden W A, Kragel P J and Hu X-H 2006 *Phys. Med. Biol.* **51**(6)1479–89
[3] WO 2013135311 A1 2012 "Method and device for imaging of spectral reflectance at several wavelength bands"
[4] Spigulis J and Elste L 2014 *Proc. SPIE* **8937** 89370L
[5] Spigulis J *Sensors* 2017 **17** 1165
[6] Spigulis J, Rupenheits Z, Matulenko M, Oshina I and Rubins U 2020 *Proc. SPIE* **11232** 112320I–1
[7] Spigulis J, Oshina I, Berzina A and Bykov A 2017 *J. Biomed.Opt.* **22**(9) 091508
[8] Lihachev A, Lihacova I, Plorina E V, Lange M, Derjabo A and Spigulis J 2018 *Biomed. Opt. Expr*. **9**(4) 1852–1858
[9] Kviesis-Kipge E 2019 *OSA Technical Digest* (Optical Society of America) ITh4B.3
[10] Lukinsone V, Maslobojeva A, Rubins U, Kuzminskis M, Osis M and Spigulis J 2020 *Biomed. Opt. Expr.* **11**(5) 2866–2873
[11] Lukinsone V, Kuzmina I, Tamosiunas M, Maslobojeva A, Kuzminskis M, Rubins U and Spigulis J 2020 *Proc. SPIE* **11363** 1136320
[12] Silveira L, Pasqualucci C A, Bodanese B, Pacheco M T T and Zângaro R A 2020 *Lasers Med. Sci.* **35** 1141–1151
[13] Feng X, Moy A J, Nguyen H T M, Zhang J, Fox M C, Sebastian K R, Reichenberg J S, Markey M K and Tunnell J W 2017 *Biomed. Opt. Expr*. **8**(6) 2835–2850
[14] Kunapareddy N, Freyer J P and Mourant J R 2008 *J. Biomed. Opt.* **13**(5) 054002
[15] Bratchenko I A, Artemyev D N, Myakinin O O, Khristoforova Y A, Moryatov A A, Kozlov S V and Zakharov V P 2017 *J. Biomed. Opt.* **22**(2) 27005
[16] Plavskii V Yu, Mikulich A V, Tretyakova A I, Leusenka I A, Plavskaya L G, Kazyuchits O A, Dobysh I I and Krasnenkova T P 2018 *J. Photochem. Photobiol.* B **183** 172–183